Research Article | Vol. 7, No. 7 | 1 Jul 2017 | OPTICAL MATERIALS EXPRESS 2672
Optical Materials EXPRESS

Volume plasmon polaritons in semiconductor hyperbolic metamaterials

DONGXIA WEI,[1] CHRISTIAN HARRIS,[2] AND STEPHANIE LAW[1,*]

[1]*Department of Materials Science and Engineering, University of Delaware, Newark DE 19716, USA*
[2]*Department of Chemistry and Physics, Lincoln University, Oxford, PA 19352, USA*
**slaw@udel.edu*

Abstract: Layered hyperbolic metamaterials are able to support bulk modes with wavevectors much larger than light in free space. These modes are the foundation of many proposed metamaterial devices. In this paper, we present experimental data measuring the dispersion relationship of these modes in infrared semiconductor hyperbolic metamaterials. The metamaterial optical properties are modeled by taking into account the functional form of the carrier density in the sample due to conduction band bending and the non-parabolicity of the effective mass. In two different samples, we observe multiple volume plasmon polariton modes, and the mode dispersion is traced out by using grating couplers with multiple periodicities. We close by discussing ways to improve these materials.

OCIS codes: (160.3918) Metamaterials; (160.6000) Semiconductor materials; (240.6680) Surface plasmons.

References and links

1. Y. Guo, W. Newman, C. L. Cortes, and Z. Jacob, "Applications of Hyperbolic Metamaterial Substrates," Adv. Optoelectron. **2012**, 452502 (2012).
2. A. Poddubny, I. Iorsh, P. Belov, and Y. Kivshar, "Hyperbolic metamaterials," Nat. Photonics **7**(12), 948–957 (2013).
3. P. Shekhar, J. Atkinson, and Z. Jacob, "Hyperbolic metamaterials: fundamentals and applications," Nano Converg **1**(1), 14 (2014).
4. L. Ferrari, C. Wu, D. Lepage, X. Zhang, and Z. Liu, "Hyperbolic metamaterials and their applications," Prog. Quantum Electron. **40**, 1–40 (2015).
5. O. Kidwai, S. V. Zhukovsky, and J. E. Sipe, "Effective-medium approach to planar multilayer hyperbolic metamaterials: Strengths and limitations," Phys. Rev. A **85**(5), 053842 (2012).
6. A. A. Krokhin, J. Arriaga, L. N. Gumen, and V. P. Drachev, "High-frequency homogenization for layered hyperbolic metamaterials," Phys. Rev. B **93**(7), 075418 (2016).
7. N. Vasilantonakis, M. E. Nasir, W. Dickson, G. A. Wurtz, and A. V. Zayats, "Bulk plasmon-polaritons in hyperbolic nanorod metamaterial waveguides," Laser Photonics Rev. **9**(3), 345–353 (2015).
8. V. E. Babicheva, M. Y. Shalaginov, S. Ishii, A. Boltasseva, and A. V. Kildishev, "Finite-width plasmonic waveguides with hyperbolic multilayer cladding," Opt. Express **23**(8), 9681–9689 (2015).
9. S. Dai, Q. Ma, T. Andersen, A. S. Mcleod, Z. Fei, M. K. Liu, M. Wagner, K. Watanabe, T. Taniguchi, M. Thiemens, F. Keilmann, P. Jarillo-Herrero, M. M. Fogler, and D. N. Basov, "Subdiffractional focusing and guiding of polaritonic rays in a natural hyperbolic material," Nat. Commun. **6**, 6963 (2015).
10. S. Ishii, A. V. Kildishev, E. Narimanov, V. M. Shalaev, and V. P. Drachev, "Sub-wavelength interference pattern from volume plasmon polaritons in a hyperbolic medium," Laser Photonics Rev. **7**(2), 265–271 (2013).
11. K. V. Sreekanth, K. H. Krishna, A. De Luca, and G. Strangi, "Large spontaneous emission rate enhancement in grating coupled hyperbolic metamaterials," Sci. Rep. **4**(1), 6340 (2015).
12. S. Thongrattanasiri and V. A. Podolskiy, "Hypergratings: nanophotonics in planar anisotropic metamaterials," Opt. Lett. **34**(7), 890–892 (2009).
13. D. Lu and Z. Liu, "Hyperlenses and metalenses for far-field super-resolution imaging," Nat. Commun. **3**, 1205 (2012).
14. A. J. Hoffman, V. A. Podolskiy, D. L. Sivco, and C. Gmachl, "Sub-diffraction negative and positive index modes in mid-infrared waveguides," Opt. Express **16**(21), 16404–16409 (2008).
15. P. Shekhar and Z. Jacob, "Strong coupling in hyperbolic metamaterials," Phys. Rev. B **90**(4), 045313 (2014).
16. S. V. Zhukovsky, A. A. Orlov, V. E. Babicheva, A. V. Lavrinenko, and J. E. Sipe, "Photonic-band-gap engineering for volume plasmon polaritons in multiscale multilayer hyperbolic metamaterials," Phys. Rev. A – At. Mol. Opt. Phys. **90**, 1–11 (2014).
17. C. L. Cortes, W. Newman, S. Molesky, and Z. Jacob, "Quantum nanophotonics using hyperbolic metamaterials," J. Opt. **14**(6), 063001 (2012).
18. I. Avrutsky, I. Salakhutdinov, J. Elser, and V. Podolskiy, "Highly confined optical modes in nanoscale metal-

#295628 https://doi.org/10.1364/OME.7.002672
Journal © 2017 Received 11 May 2017; revised 21 Jun 2017; accepted 23 Jun 2017; published 29 Jun 2017

Optical Materials EXPRESS

dielectric multilayers," Phys. Rev. B **75**, 241402(R) (2007).
19. S. V. Zhukovsky, O. Kidwai, and J. E. Sipe, "Physical nature of volume plasmon polaritons in hyperbolic metamaterials," Opt. Express **21**(12), 14982–14987 (2013).
20. P. Berini, "Long-range surface plasmon polaritons," Adv. Opt. Photonics **1**(3), 484 (2009).
21. T. Søndergaard and S. I. Bozhevolnyi, "Strip and gap plasmon polariton optical resonators," Phys. Status Solidi **245**(1), 9–19 (2008).
22. J. Jung, T. Søndergaard, and S. I. Bozhevolnyi, "Gap plasmon-polariton nanoresonators: Scattering enhancement and launching of surface plasmon polaritons," Phys. Rev. B **79**(3), 035401 (2009).
23. J. Schilling, "Uniaxial metallo-dielectric metamaterials with scalar positive permeability," Phys. Rev. E Stat. Nonlin. Soft Matter Phys. **74**(4), 046618 (2006).
24. L. Sun, Z. Li, T. S. Luk, X. Yang, and J. Gao, "Nonlocal effective medium analysis in symmetric metal-dielectric multilayer metamaterials," Phys. Rev. B **91**(19), 195147 (2015).
25. S. V. Zhukovsky, A. Andryieuski, J. E. Sipe, and A. V. Lavrinenko, "From surface to volume plasmons in hyperbolic metamaterials: General existence conditions for bulk high-k waves in metal-dielectric and graphene-dielectric multilayers," Phys. Rev. B **90**(15), 155429 (2014).
26. K. V. Sreekanth, A. De Luca, and G. Strangi, "Excitation of volume plasmon polaritons in metal-dielectric metamaterials using 1D and 2D diffraction gratings," J. Opt. **16**(10), 105103 (2014).
27. S. Law, R. Liu, and D. Wasserman, "Doped semiconductors with band-edge plasma frequencies," J. Vac. Sci. Technol. B **32**(5), 52601 (2014).
28. S. Law, L. Yu, and D. Wasserman, "Epitaxial growth of engineered metals for mid-infrared plasmonics," J. Vac. Sci. Technol. B **31**, 03C121 (2013).
29. S. Law, D. C. Adams, A. M. Taylor, and D. Wasserman, "Mid-infrared designer metals," Opt. Express **20**(11), 12155–12165 (2012).
30. M. Shahzad, G. Medhi, R. E. Peale, W. R. Buchwald, J. W. Cleary, R. Soref, G. D. Boreman, and O. Edwards, "Infrared surface plasmons on heavily doped silicon," J. Appl. Phys. **110**(12), 123105 (2011).
31. J. C. Ginn, R. L. Jarecki, Jr., E. A. Shaner, and P. S. Davids, "Infrared plasmons on heavily-doped silicon," J. Appl. Phys. **110**(4), 043110 (2011).
32. T. Taliercio, V. N. Guilengui, L. Cerutti, J. B. Rodriguez, F. Barho, M. J. Rodrigo, F. Gonzalez-Posada, E. Tournié, M. Niehle, and A. Trampert, "Fano-like resonances sustained by Si doped InAsSb plasmonic resonators integrated in GaSb matrix," Opt. Express **23**(23), 29423–29433 (2015).
33. V. N. Guilengui, L. Cerutti, J. B. Rodriguez, E. Tournie, and T. Taliercio, "Localized surface plasmon resonances in highly doped semiconductors nanostructures," Appl. Phys. Lett. **101**(16), 161113 (2012).
34. A. J. Hoffman, L. Alekseyev, S. S. Howard, K. J. Franz, D. Wasserman, V. A. Podolskiy, E. E. Narimanov, D. L. Sivco, and C. Gmachl, "Negative refraction in semiconductor metamaterials," Nat. Mater. **6**(12), 946–950 (2007).
35. A. J. Hoffman, A. Sridhar, P. X. Braun, L. Alekseyev, S. S. Howard, K. J. Franz, L. Cheng, F. Sen Choa, D. L. Sivco, V. A. Podolskiy, E. E. Narimanov, and C. Gmachl, "Midinfrared semiconductor optical metamaterials," J. Appl. Phys. **105**(12), 122411 (2009).
36. D. Wei, C. Harris, C. C. Bomberger, J. Zhang, J. Zide, and S. Law, "Single-material semiconductor hyperbolic metamaterials," Opt. Express **24**(8), 8735–8745 (2016).
37. D. Blazek, M. Cada, and J. Pistora, "Surface plasmon polaritons at linearly graded semiconductor interfaces," Opt. Express **23**(5), 6264–6276 (2015).
38. G. Snider, "1D Poisson," http://www3.nd.edu/~gsnider/.
39. M. Cardona, "Electron Effective Masses of InAs and GaAs as a Function of Temperature and Doping," Phys. Rev. **121**(3), 752–758 (1961).
40. W. G. Spitzer and H. Y. Fan, "Determination of Optical Constants and Carrier Effective Mass of Semiconductors," Phys. Rev. **106**(5), 882–890 (1957).

1. Introduction

In comparison to normal materials, which exhibit closed isofrequency surfaces, hyperbolic metamaterials (HMMs) have open hyperbolic isofrequency surfaces that can support the propagation of optical modes with wavevectors much larger than light in free space [1–4]. One way to create an HMM is by constructing a superlattice of alternating subwavelength metal and dielectric layers. The optical properties of the superlattice can be described by effective medium theory so long as the layers are much thinner than the wavelength of light [5,6]. The HMM has effective parallel (in the plane) and perpendicular (out of the plane) permittivities given by

$$\varepsilon_{\parallel}(\omega)=\frac{\varepsilon_m(\omega)+\eta\varepsilon_d}{1+\eta} \qquad \varepsilon_{\perp}(\omega)=\frac{1+\eta}{\frac{1}{\varepsilon_m(\omega)}+\frac{\eta}{\varepsilon_d}} \tag{1}$$

Optical Materials EXPRESS

where ω is the frequency of the light, $\varepsilon_m(\omega)$ and ε_d are the permittivities of the metal and dielectric layers, respectively, and $\eta = t_d / t_m$ is the ratio of their thicknesses. For a correctly-designed structure, there will be bandwidths over which $\varepsilon_{\parallel} < 0$ and $\varepsilon_{\perp} > 0$ or vice versa. This difference in sign leads to the aforementioned open hyperbolic isofrequency surface. This open surface allows light with a large wavevector to propagate in the material, rather than decay exponentially close to the surface. These high-wavevector modes can be used for a variety of applications, including enhanced sensing, emission control, waveguiding, strong coupling, and subwavelength imaging and focusing [7–17].

At a fundamental level, these large-wavevector modes arise from the coupling of surface plasmon polaritons (SPPs) at every metal/dielectric interface in the superlattice [18,19]. In a single subwavelength metallic layer surrounded by dielectric materials, two SPPs can be excited: one on the top surface and one on the bottom surface. When the dielectrics on either side of the metallic layer are identical and the metallic layer is much thinner than the wavelength of light, these SPPs can couple into symmetric and antisymmetric modes. These are sometimes called long-range plasmon polaritons and short-range plasmon polaritons, respectively [20]. For the inverse case of two metallic films separated by a thin subwavelength dielectric, the SPPs excited at each metal/dielectric interface can couple across the dielectric. Symmetric and antisymmetric modes are again excited, with the symmetric mode sometimes referred to as a "gap plasmon" [21,22]. As more layers are added to the structure, more interfaces are created, and the structure can support complex large-wavevector modes. These large-wavevector modes have been called by a variety of names, including multilayer plasmons [23], bulk plasmon polaritons [7,18,24], and volume plasmon polaritons (VPPs) [2,10,16,19,25,26]. We will adopt the latter terminology in this paper. A structure with four metal layers can support a maximum of three VPPs in addition to the long- and short-range plasmon polaritons [18]. These modes will have zero, one, or two nodes in the magnetic field profile as a function of depth and exhibit wavevectors many times larger than light in free space. The maximum number of VPP modes present in an ideal structure will always be one less than the number of metallic layers. However, a real structure will always have a maximum wavevector beyond which the VPP modes cannot exist. This happens when the size of the VPP wavevector becomes comparable to the size of the layers comprising the HMM and the modes no longer experience a homogeneous effective medium. In order to excite the large-wavevector VPP modes, we must add momentum to the incident photons. One way to add momentum is through a metallic grating coupler [26], which increases the wavevector of the light by $2\pi / \Lambda$, where Λ is the period of the grating. The ratio of momentum in the plane of the HMM (k_x) to the momentum of incident light (k_o) can be expressed as:

$$\frac{k_x}{k_o} = \sin\theta + \frac{\lambda}{\Lambda} \tag{2}$$

where θ is the incident angle, and λ is the wavelength of incident light. In our study, multiple pieces from the same HMM chip are fabricated with different grating periods to map out the dispersion of the VPP modes.

Doped semiconductors have previously been shown to be good plasmonic materials in the infrared [27–33]. The carrier density can easily be controlled in these materials, leading to tunable optical properties across wide bandwidths. III-V semiconductors like InAs and InGaAs can be grown by molecular beam epitaxy (MBE), an ultra-high vacuum technique in which the materials are grown one atomic layer at a time. MBE is well-known as an excellent technique for the growth of superlattices and is a natural way to create a layered semiconductor HMM [14,34,35]. In our previous work, we created HMMs using a single semiconductor material system: doped InAs for the metallic components and undoped InAs

Optical Materials EXPRESS

for the dielectric components [36]. We demonstrated discontinuity of the Brewster angle as well as negative refraction, both hallmarks of an HMM. The samples described in that work are used in this manuscript as well. In this paper, we report on our efforts to excite VPP modes in semiconductor HMMs and map out their dispersion. Due to their large wavevectors, VPP modes are particularly exciting for infrared applications including waveguiding, imaging, and focusing. Before we can harness VPPs in infrared devices, we must understand how to model and measure them in real materials. In this paper, we discuss how to model these materials while including band bending at the interfaces. We then show experimental data demonstrating our ability to excite VPP modes in single-material semiconductor HMMs; to our knowledge, this is the first demonstration of VPP modes in the infrared. We use a grating to couple into the VPP modes, and by changing the period of the grating, we are able to experimentally map out the dispersion of these modes. We close by discussing ways to improve these materials.

2. Experimental setup

The samples used for these experiments were grown by molecular beam epitaxy (MBE) and their unpatterned bulk optical properties previously reported in [36]. In this article, we report VPPs excited in Sample 1 and Sample 3 from our previous paper; we keep the same nomenclature in this report for simplicity. Sample 1 has metal and dielectric layers with thicknesses of 110nm, a plasma wavelength in the doped layers of 5.8μm, and a scattering rate in the doped layers of $1.9\text{x}10^{13}$ s^{-1}. Sample 3 has metal and dielectric layers with thicknesses of approximately 90nm and 110nm, respectively, a plasma wavelength in the doped layers of 9.5μm, and a scattering rate in the doped layers of $1.4\text{x}10^{13}$ s^{-1}. The plasma frequency and scattering rate are determined using far-field measurements and effective medium theory. For both samples, GaAs substrates are used, followed by a 500nm undoped InAs buffer layer to account for the difference in lattice constant between the substrate and the HMM. The HMM is grown with ten repeats of the doped and undoped layers, for a thickness in Samples 1 and 3 of 2.8μm and 2.4μm, respectively. Details of the growth process can be found in [36]. Standard electron-beam lithography, electron-beam deposition, and liftoff techniques are used to create Ti/Au gratings on top of the samples. The thickness of the gold grating is 100nm with a 15nm Ti adhesion layer on the bottom. Each HMM superlattice ends with an undoped InAs layer, separating the metal gratings from the doped semiconductor layers by ~100nm. A combination of SEM and optical microscopy were used to verify the grating period, stripe width, height, and sidewall profile.

After fabrication, the optical properties of the samples are measured. TM- and TE-polarized reflection spectra are taken using a Bruker Vertex 70V Fourier transform infrared (FTIR) spectrometer with a wide-range DTGS detector and a KRS-5 holographic wire grid polarizer. A Pike 10spec accessory whose reflection angle is set to be 10 degrees for both the incident and collected light enables us to take specular reflection data inside the sample compartment. A gold mirror is used to collect polarized background spectra. The scan velocity is 2.5 kHz and the scan resolution is 2cm^{-1}.

3. Modeling

Due to the small conduction band offset in the Si:InAs/InAs superlattice, electrons are not always well-confined to the Si:InAs layer. As previously discussed, VPPs arise from coupled SPPs excited at each interface in the superlattice. The precise shape of the interface significantly affects the properties of the VPPs. To model our samples accurately, we must consider the actual shape of the conduction band as a function of depth [37]. The first step in our modeling process is to use a one-dimensional self-consistent Poisson solver (*1D Poisson* made freely available by G. Snider [38]) to study the shape of the conduction band and resulting electron distribution inside the structure. The modeling assumes ideal structural parameters: the electron density in the doped regions is equal to the density of silicon donor

Optical Materials EXPRESS

atoms and the thicknesses of the doped and undoped layers are as designed. The plasma wavelength in the doped regions is calibrated with FTIR measurements on thick silicon-doped InAs films.

Results from this modeling for Sample 1 are shown in Fig. 1(a). Sample 3 is similar. The conduction band shows a clear transition area between the heavily doped regions and the undoped regions. The carrier density is therefore not a square-wave type function, but a more complex function of position. We can study the structure by separating it into three areas as denoted in Fig. 1(a): uniformly doped areas denoted with an "a," graded areas shaded in gray and denoted with a "b," and undoped areas denoted with a "c." To model the shaded regions accurately, we need a functional form for the carrier density as a function of depth. We find empirically that the Boltzmann equation fits well. For example, the following equation describes the graded area of Sample 1 where the electron doping density changes from high to low:

$$n(z) = n_{\max}\left(-0.5226 + \frac{1.5170}{1+\exp\left(\frac{z-225.5435}{38.8166}\right)}\right) \tag{3}$$

where $n_{\max}$ is the maximum doping density ($7.35\text{x}10^{19}$ cm^{-3} for Sample 1 and $1.25\text{x}10^{19}$ cm^{-3} for Sample 3). This fitting equation was normalized to the maximum doping density in section "a" to allow us to use the same equation to fit multiple samples. Now that we have an accurate functional form describing how the carrier density changes as a function of depth, we can use this to simulate the optical properties of our samples.

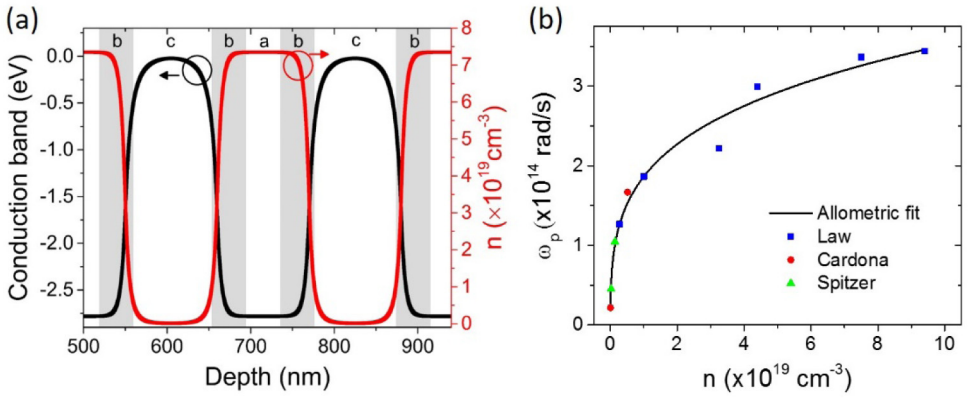

Fig. 1. (a) Conduction band profile (black) and carrier density (red) in the Si:InAs/InAs superlattice from Sample 1 as calculated using a self-consistent Poisson solver. In region a, the material is modeled as a Drude metal with a constant carrier density, while in region c, the material is modeled as undoped InAs with a constant permittivity of 12.3. In the shaded region b, the carrier density depends on depth as described below. (b) Experimental (symbols) and empirical model (black line) for plasma frequency as a function of carrier density in doped InAs. Data from [29].

We used COMSOL Multiphysics 5.2a, a commercial finite element modeling program, to simulate the reflection from our grating-coupled HMMs at a 10 degree incident angle using mesh sizes ranging from 0.01nm to 12nm inside the sample. A built-in Drude-Lorentz dispersion model is used to model the optical properties of both the uniformly doped and graded areas. COMSOL requires the plasma frequency and scattering rate as inputs for each material. For area "a" as denoted in Fig. 1(a), the plasma frequency is constant and is determined through calibration films as well as modeling of the unpatterned samples, as

Optical Materials EXPRESS

described in detail in [36]. Values for Samples 1 and 3 are given in Section 2. Area "c" is modeled as a dielectric with permittivity equal to the high frequency permittivity of InAs, 12.3. However, in area "b," the doping density varies with depth, which will cause the plasma frequency to vary with depth. Unfortunately, a simple Drude model relationship between the plasma frequency and the carrier density is not appropriate for these materials, because the effective mass in InAs is highly non-parabolic and thus is also a function of carrier density. Instead, we developed a semi-empirical equation to describe the relationship between doping density and plasma frequency. We took data from three references [27,39,40] that give the plasma frequency for a variety of carrier densities in doped InAs. This data is plotted as symbols in Fig. 1(b). We then used the following equation to fit the data

$$\omega_p(n) = -4.5433\times10^{13} + 8.44\times10^{9}\times n^{0.23363} \tag{4}$$

In this equation, ω_p has units of rad/s while n has units of cm^{-3}. It should be emphasized that this equation includes the effects of the non-parabolic effective mass and is only applicable for samples with carrier densities between ~$5x10^{16}$-$1x10^{20}$ cm^{-3}. Using this equation in combination with Eq. (3) describing the carrier density as a function of depth, we can describe the plasma frequency as a function of depth in the graded areas. This enables us to use COMSOL to simulate the TE and TM reflection spectra for Samples 1 and 3 using the real depth-dependent carrier profile. Further details on the modeling are available in Appendix 1.

4. Results and discussion

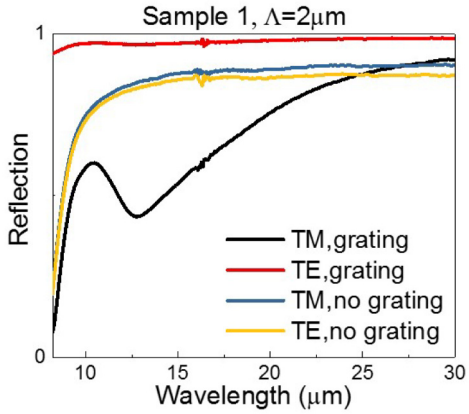

Fig. 2. Reflection spectra for Sample 1 without a grating (blue and yellow) and with a grating (black and red) for both TM (black and blue) and TE (red and yellow) polarized light. For both polarizations without the grating and for TE-polarized light with the grating, no VPP modes are observed. Only for TM-polarized light with the grating are long-wavelength VPP modes visible.

Figure 2 shows TM- and TE-polarized reflection data for Sample 1 both with and without a $\Lambda = 2\mu m$ gold grating coupler. Data is presented only for the type II HMM region where $\varepsilon_{\parallel} < 0$ and $\varepsilon_{\perp} > 0$. Other samples show similar behavior. The TM- and TE-polarized data without the grating, shown in blue and yellow respectively, show high reflectivity across this spectral range, as expected for a type II HMM. The TE-polarized reflection data with the grating (red curve) also shows a large reflectivity, again as expected since TE-polarized light will not excite the VPP modes. Finally, the TM-polarized data with the grating (black) shows a clear absorption feature near 12.5μm. As will be discussed later, this can be attributed to two overlapping VPP modes. It should be noted that these features are not simply diffraction

resonances from the grating. For a grating with a 2μm period and incident and reflected angles of 10 degrees, all grating resonances are at wavelengths of 0.7μm and shorter. For a grating with a 4.6μm period (the largest used in this study), all grating resonances are at wavelengths of 1.6μm and shorter. The grating is only used to add momentum to the light in order to excite the VPP modes. It should also be noted that the overall goal of this project is to understand the VPP modes in semiconductor HMMs. The grating parameters (material, thickness, stripe width, and separation from the HMM) were not optimized. A systematic walk through parameter space would almost certainly result in a more efficient grating coupler. However, as discussed below, the grating parameters used in this project were sufficient to excite VPP modes and measure their dispersion.

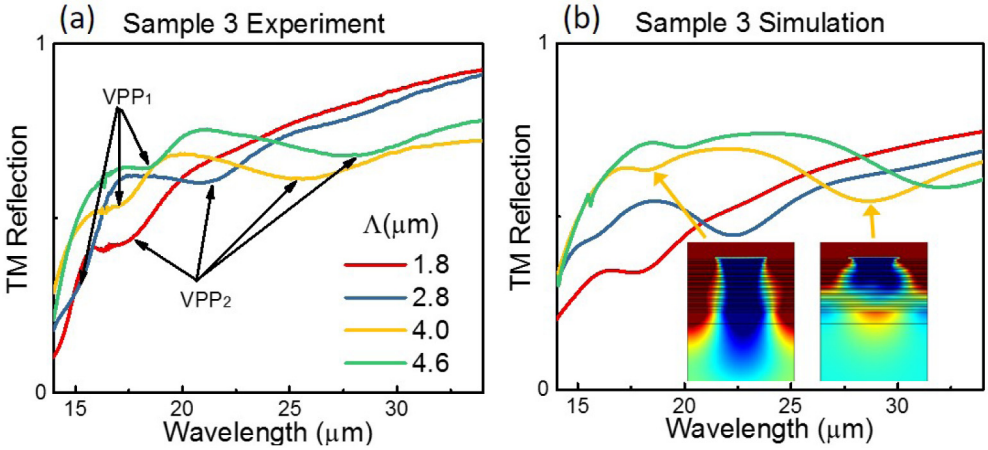

Fig. 3. (a) Experimental and (b) simulated TM-polarized reflection from Sample 3 for four different period gratings, as indicated in the legend. VPP modes are clearly visible and marked with arrows in (a). In (b), the out-of-plane magnetic field profile is shown for two VPP modes. The shorter wavelength resonance has no nodes, while the longer wavelength resonance has one node, as expected for VPPs.

In Fig. 3(a), we show experimental TM-polarized reflection data for Sample 3 with four different gratings whose periods range from 1.8μm to 4.6μm. Two clear VPP resonances are visible and are marked with arrows. A third, longer wavelength VPP mode is present in the 1.8μm and 2.8μm samples. This mode is not clearly visible in the other samples, as its expected resonant wavelength overlaps with the optical phonon band for InAs. As the grating period increases, the VPP modes shift to longer wavelengths. In Fig. 3(b), we show the TM-polarized reflection data for Sample 3 simulated using COMSOL. This simulation takes into account the real electron distribution in the sample and the empirical dependence of plasma wavelength on carrier density, as described in Section 3. The carrier density and conduction band profiles remain constant as the wavevector is changed. In this model, no fitting parameters are used. The maximum carrier density is known and a single scattering rate is used throughout the uniformly doped and graded areas. Despite the lack of fitting parameters and the complexity of the shape of the interface, the simulation reproduces the salient features of the data. The VPP modes are clearly visible and shift to longer wavelengths as the period increases. The features are, however, red-shifted in the model compared to the experiment. We attribute this mainly to the difficulty in knowing the precise electron distribution in the sample. Small changes in the electron distribution or the maximum electron density can strongly affect the precise position of these resonances. Rather than arbitrarily changing the electron distribution to match our data, we opted to use the model as described above. In addition to simulating the TM-polarized reflection, we are also able to extract the out-of-plane magnetic field profile in the sample. Two example profiles at the VPP resonant wavelengths are shown as insets in Fig. 3(b). The shorter wavelength mode has no nodes in the magnetic

Optical Materials EXPRESS

field, while the longer wavelength mode has one node. This is as expected for VPP modes, where each subsequent higher-order (lower-energy) mode has one more node in the magnetic field [18]. These profiles indicate that we are, indeed, observing VPP modes.

In Fig. 4(a) and (b), experimental and simulated TM-polarized reflection data for Sample 1 are shown. Again, the simulation reproduces the relevant features of the experimental data, though the VPP modes are still redshifted in the simulation with respect to the experiment. These modes occur at shorter wavelengths than those observed in Sample 3, since Sample 1 has a higher doping density and thus a transition to type II HMM behavior at shorter wavelengths. In this case, two VPP modes are present, but they are not well-separated; the resonance widths are larger than the mode spacing. The existence of two VPP modes is easier to see in the modeled data where there are two distinct dips.

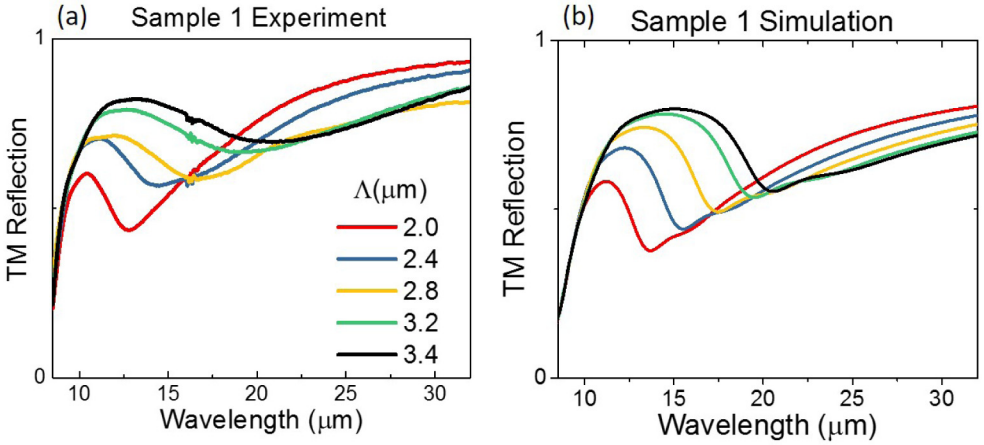

Fig. 4. (a) Experimental and (b) simulated TM-polarized reflection from Sample 1 for five different period gratings, as indicated in the legend. Two VPP modes are visible, though they are not well-separated.

In order to understand the dispersion of these modes, we must extract the positions of the VPP resonances and plot them as a function of wavevector. For Sample 3, this is relatively straightforward, as the VPP modes are well-separated. However, for Sample 1, the overlapping modes make this more difficult. To extract the peak positions, we fitted the spectra in Figs. 3 and 4 with multiple Lorentzians. For Sample 1, two Lorentzians were needed to fit the data, while for Sample 3, three Lorentzians were used for all spectra except the experimental 4.0μm and 4.6μm grating samples. The third VPP resonance was not clearly observed for these samples due to interference from the InAs optical phonons. More modes are visible in Sample 3 compared to Sample 1. This is likely due to the larger scattering rate in Sample 1 resulting from its higher doping density. The modeling results in Appendix 1 clearly show that the scattering rate has a strong effect on the number of visible VPP modes.

After the resonant wavelengths were extracted, the wavevector was calculated as described in Eq. (2). The dispersion curves are shown in Fig. 5. For both samples, the experimental data is at a smaller k_x / k_o than predicted. We attribute this mismatch to the difficulty in knowing the exact distribution of carriers in the sample as a function of depth as well as an imperfect model for how the plasma frequency depends on carrier density. Despite the imperfect match between experiment and modeling, both sets of dispersion curves show the expected dependence for VPP modes. In the case of Sample 3, we are able to experimentally excite VPP modes with wavevectors an order of magnitude larger than free space.

Optical Materials EXPRESS

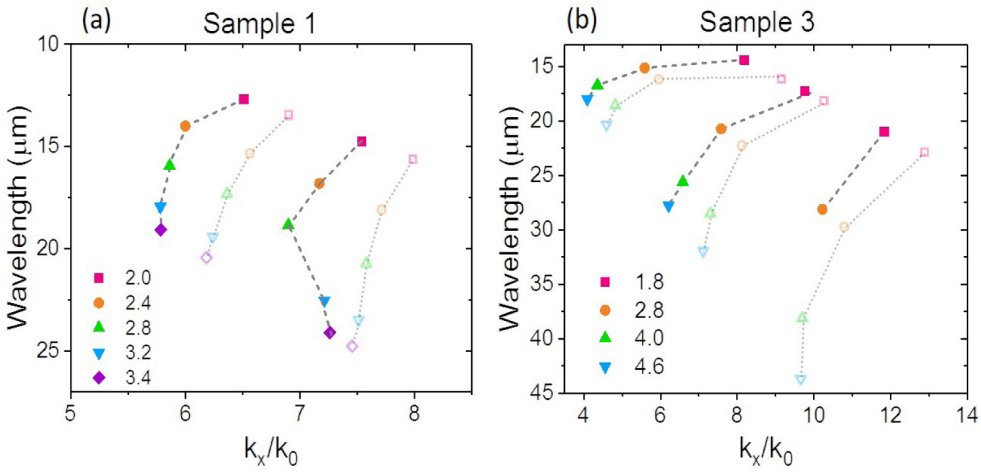

Fig. 5. Dispersion relations for VPP modes for experimental (filled symbols) and simulated (open symbols) data for Sample 1 (a) and Sample 3 (b). Lines are a guide to the eye.

In the future, more well-separated VPP modes could be accessed in samples with a larger conduction band offset between the doped and undoped regions, such as Si:InGaAs/InAlAs or Si:InAs/GaSb. In these material systems, the carriers will be more strongly confined to the doped regions, eliminating the graded transition region between the doped and undoped material layers. These sharper interfaces will, in turn, result in sharper VPP modes, as confirmed by the modeling shown in Appendix 1. It may also be possible to design a more efficient grating coupler by adjusting the material or the grating width or height. Nevertheless, in this very simple system we have clearly excited VPP modes in semiconductor HMMs with wavevectors an order of magnitude larger than the light used to excite them.

5. Conclusions

In summary, we have fabricated grating couplers with a range of periods on semiconductor hyperbolic metamaterials to excite volume plasmon polariton modes and map their dispersion relationship. Reflection measurements were performed on these samples and resonances observed only for TM-polarized reflection with the grating coupler, as expected for VPP modes. We used a self-consistent Poisson solver to model the carrier density as a function of depth and developed an empirical model to describe the plasma wavelength as a function of carrier density in doped InAs, accounting for the carrier-dependent effective mass. These models were then used as inputs to allow us to model the reflection from our samples using COMSOL. The model reproduced the relevant experimental features well, though the resonant positions were red-shifted. We extracted magnetic field profiles for these large-wavevector resonances and found that they were consistent with those expected for VPP modes. Finally, we plotted the VPP mode dispersion and demonstrated the ability to excite modes with wavevectors an order of magnitude larger than light in free space. The dispersion relationships shown are consistent with VPP modes. Now that these modes have been observed and characterized, they can be harnessed for applications in subwavelength focusing, waveguiding, and the improvement of infrared emitters and detectors.

Optical Materials EXPRESS

6. Appendix 1

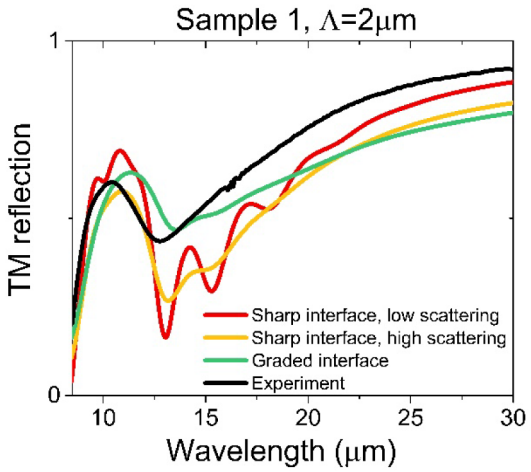

Fig. 6. Comparison of models for TM-polarized reflection for Sample 1 with a 2μm period grating. Experimental data is shown in black, modeled reflection assuming a sharp interface with low scattering ($\Gamma = 2x10^{13}$ rad/s) is shown in red, a sharp interface with high scattering ($\Gamma = 4x10^{13}$ rad/s) is shown in yellow, and the graded interface is shown in green.

In Fig. 6, we show experimental TM reflection data in black as well as modeled reflection data using a variety of carrier density profiles for Sample 1 with a grating with period 2μm. When first attempting to fit the experimental data, we assumed a sharp interface between the doped and undoped layers. The simulated TM-reflection obtained using this sharp interface model is plotted as the red and yellow curves. The red curve has a lower scattering rate ($\Gamma=2x10^{13}$ rad/s) while the yellow curve has a higher scattering rate ($\Gamma=4x10^{13}$ rad/s). The red curve clearly shows many strong, well-separated VPP modes. As the scattering rate is increased in the yellow curve, the VPP features decrease in strength, with some weaker modes disappearing entirely. However, it is clear that regardless of the scattering rate, neither of these sharp-interface models will reproduce the experimental data well. The green curve plots the simulated TM-reflection using the graded interface model as described in Section 3 of the main text. The VPP features near 12μm and 15μm have broadened and overlapped, similar to what is observed in the experimental data, and the qualitative shape of the reflection curve has changed. As described in the main text, this graded interface model uses no fitting parameters other than the maximum carrier density and scattering rate, which are obtained from other measurements. Despite the imperfect fit with the experimental data, the agreement in the overall shape of the curves makes it clear that the graded interface model is a much more accurate way to describe our samples.

Funding

National Science Foundation (NSF) (1606673).